



Designed $\text{SO}_4^{2-}/\text{Fe}_2\text{O}_3\text{-SiO}_2$ solid acids for polyoxymethylene dimethyl ethers synthesis: The acid sites control and reaction pathways

Huaju Li^{a,b}, Huanling Song^b, Liwei Chen^c, Chungu Xia^{b,*}

^a Laboratory for Nano-catalytic Material & Technology, Division of Advanced Nano-materials, Suzhou Institute of Nano-Tech and Nano-Bionics, Chinese Academy of Sciences, Suzhou 215123, China

^b State Key Laboratory for Oxo Synthesis and Selective Oxidation, Lanzhou Institute of Chemical Physics, Chinese Academy of Sciences, Lanzhou 730000, China

^c i-LAB, Suzhou Institute of Nano-Tech and Nano-Bionics, Chinese Academy of Sciences, Suzhou 215123, China

ARTICLE INFO

Article history:

Received 1 July 2014

Received in revised form

23 September 2014

Accepted 11 October 2014

Available online 22 October 2014

Keywords:

Polyoxymethylene dimethyl ethers

Pyridine-IR

Acid strength

In situ DRIFTS

TPD

ABSTRACT

The designed model $\text{SO}_4^{2-}/\text{Fe}_2\text{O}_3\text{-SiO}_2$ catalysts with varied acidic strength and Brønsted acid sites were successfully prepared. The properties of acid sites can be regulated by preparation method and silica incorporation. The S/Fe sample without silica had stronger acid strength, more Brønsted acid sites and higher acid density, which showed the best catalytic performance. NH_3 -TPD, pyridine-IR and methanol/dimethoxymethane adsorption-desorption techniques were employed to reveal the relationship between acid properties of the catalysts and catalytic activity for the reaction of trioxane with methanol. Further, this reaction is determined by the strength of acid sites on catalyst surface and does not affect by the inner pore diffusion. These findings suggest that the catalytic activity and selectivity can be monitored mainly by acid strength and Brønsted acid sites on the sulfated oxides, while trioxane decomposition process seems to be a vital step and polyoxymethylene hemiacetals are supposed to be the key intermediates. Meanwhile, a large number of acid sites and a higher surface area of the catalysts can also improve the catalytic performance. These results should provide some specific guidance for understanding of the reaction mechanism and the catalyst design.

© 2014 Elsevier B.V. All rights reserved.

1. Introduction

Diesel fueled engines play important roles and have revolutionized transportation worldwide, meanwhile release large amount of exhaust gases that is still a serious problem remains unsolved, even in modern society. Both petroleum shortage and environmental concern provoke technique innovations to reduce soot formation, e.g., fuel additives (oxygenated compounds) are commonly considered to be the feasible route to promote fuel efficiency and reduce soot formation during the combustion [1]. The polyoxymethylene dimethyl ethers (DMM_n) with the structure of $\text{CH}_3\text{-O-(CH}_2\text{O)}_n\text{-CH}_3$ have lower vapor pressures, higher viscosities, and higher cetane numbers [2], which are much more promising blending components for clean oils, especially for diesel fueled engines, compared to dimethyl ether (DME) [3] and methylal (DMM) [4–6]. In addition, DMM_n can be obtained from methanol

and its downstream products (formaldehyde, trioxane, DME, DMM, etc.), and thus have the potential scientific values and application prospects for petrochemical and methanol industry.

Thus far, there were lots of articles about the synthesis of DMM_n ($n=1$) [7–9], but only a few reports for the synthesis of DMM_n ($n>1$) [10–14], due to the complex reactions and lots of products involved. The thermodynamic feasibility for DMM_n synthesis from methanol/DME and formaldehyde/trioxane etc. was reported that based on theoretical calculations [15]. In fact, the DMM_n production is realized by acid catalyzed process, by which ion exchange resins [2], ionic liquids [10,11], molecule sieves [16], solid superacids [17], etc. are employed. Zhao et al. [16] reported that the selectivity of DMM_n with different chain lengths and the conversion of trioxane were obviously different, because of varied acidic properties of the molecular sieves. Recently, Burger et al. published a series of papers for DMM_n synthesis from trioxane and DMM, in which the chemical equilibrium, reaction kinetics, and chemical process design were intensively investigated [2,18–20]. Also, they discussed the DMM_n chain length distribution in different reaction conditions and confirmed that all the reactions were equilibrium reactions, in

* Corresponding author. Tel.: +86 931 4968089.
E-mail address: cgxia@licp.cas.cn (C. Xia).

accordance with the results that previously suggested by Arvidson et al. [21].

The catalytic activity have been extensively investigated according to published reports, however, the structure–activity relationship that determines the reaction pathway is seldom studied, because of the complex reaction process and varied products. Essentially, this reaction contains the process of carbon chain growth and termination, while catalyst design is the core technique to regulate the two processes in order to obtain the desired products. Furthermore, well understanding the key step and/or intermediates of this reaction would be favorable for the catalysts design. Recently, we found that the $\text{SO}_4^{2-}/\text{Fe}_2\text{O}_3$ catalyst had a good activity and stability for synthesis of DMM_n from methanol and trioxane, and then the reaction conditions were optimized [17]. In addition, the sulfate species has no promoting effect on SiO_2 and could not generate strong acidity [22], and thus, it can be concluded that SiO_2 -doping could change the acid strength of $\text{SO}_4^{2-}/\text{Fe}_2\text{O}_3$. In the present work, we examined the relationship between acid properties and reaction activities of trioxane with methanol over SiO_2 modified model $\text{SO}_4^{2-}/\text{Fe}_2\text{O}_3$ solid acids, in order to better understand the active acid sites that generated by the interaction between sulfate species and iron oxides for DMM_n formation.

2. Experimental

2.1. Catalyst preparation

The $\text{SO}_4^{2-}/\text{Fe}_2\text{O}_3\text{-SiO}_2$ catalysts were synthesized by the conventional two-step method as described elsewhere [17]. Typically, 80.8 g $\text{Fe}(\text{NO}_3)_3 \cdot 9\text{H}_2\text{O}$ was dissolved in 200 mL water; followed by the addition of 25% aqueous ammonia under vigorous stirring until the final pH of the solution was adjusted to 9, and then required amount of silica sol was added in order to obtain the desired Fe/Si mixed oxide supports. The precipitate was further aged for 6 h in the mother liquid; in addition, the precursor that hydrothermally treated at 373 K for 12 h was named as Fe-HT; after filtrating and being washed with water, the resultant solid was dried at 373 K for 12 h. Subsequently, the powder was suspended in sulfuric acid solution (0.5 mol/L, 15 mL for 1 g of the powder) for 2 h, the powder was filtered, dried overnight at 373 K and then calcined at 773 K for 5 h. The $\text{SO}_4^{2-}/\text{Fe}_2\text{O}_3$ solid acids prepared by simple aging and hydrothermal treatment were expressed as S/Fe and S/Fe-HT, while the varied amount of silica-added catalysts were termed as S/Fe-Si-1 and S/Fe-Si-2, respectively.

2.2. Characterization

N_2 adsorption–desorption isotherms were recorded at 77 K by using a TriStar II 3020 instrument (Micromeritics). Before the measurements, all the samples were degassed at 573 K for 4 h to remove moisture and volatile impurities, and the specific surface areas were calculated by using the Brunauer–Emmett–Teller (BET) method. The pore-size distribution curves were determined by the Barrett–Joyner–Halenda (BJH) method according to the adsorption branch of the isotherms.

Scanning electron microscopy (SEM) images were obtained on a FEI Quanta 250 microscope equipped with an energy dispersive X-ray (EDX) analyzer for elemental analysis on a microscopic scale. The elemental analyses were measured by X-ray fluorescence (XRF) spectrum analyzer on a Magix PW2403 (PANalytical, Inc.). Power X-ray diffraction (XRD) patterns were recorded on a Bruker D8 Advance X-ray diffractometer using $\text{Cu K}\alpha$ radiation operated at 40 kV and 40 mA.

Hydrogen temperature-programmed reduction (H_2 -TPR-MS) was measured using an AMETEK (LC-D-200 Dycor AMETEK) mass

spectrum. 100 mg samples were pretreated with N_2 at 573 K for 0.5 h. After cooling down to room temperature and introducing a 5% H_2/Ar mixture (50 mL min^{-1}), the temperature was then programmed to rise at a ramp of 10 K min^{-1} . CH_3OH and DMM adsorption and temperature-programmed desorption (TPD) were also carried out using the same instrument by following the similar procedures.

Temperature-programmed desorption of ammonia (NH_3 -TPD) was carried out using an Autochem II 2920 instrument (Micromeritics) analyzed with a thermal conductivity detector (TCD). 100 mg samples were heated to 573 K at a rate of 10 K min^{-1} , and maintained at the temperature for 0.5 h under Ar flow (30 mL min^{-1}), after cooling down to 373 K and introducing a 10% NH_3/Ar gas mixture (20 mL min^{-1}) for 20 min. Subsequently, the physisorbed ammonia was removed by purging the sample with Ar (30 mL min^{-1}) at 373 K for 1 h, then the sample was heated to 873 K at a rate of 10 K min^{-1} under Ar flow (30 mL min^{-1}).

Diffuse reflection infrared Fourier transform spectroscopy (DRIFTS) spectra were collected over a Nicolet 6700 spectrometer (ThermoFisher) equipped with a MCT-A detector. The adsorption of pyridine was performed using a DRIFTS chamber (Smart collector II, Thermo spectra-tech), allowing thermal treatments under controlled atmospheres. The sample was pretreated under vacuum at 673 K for 4 h, the pyridine was introduced until saturation after cooling to room temperature, subsequently. After purged with He and evacuated, the sample was raised to 423 K at which the spectra was obtained. The blank experiments were operated under the same conditions that were used as the background to insure the accuracy of the infrared spectra of pyridine adsorption. The Brønsted and Lewis acidity were obtained according to the method proposed by Basila et al. [23], and the bond order of $\text{S}=\text{O}$ was calculated by the equation suggested by Jin et al. [22].

2.3. Reaction performance test

The reaction activity tests were carried out in a 150 mL stainless steel autoclave at a stirring speed of 400 rpm under the following reaction conditions: 39.2 g trioxane, 20.8 g methanol, and 0.9 g catalyst, 403 K for 2 h. After being purged by N_2 , the reactor was heated to the reaction temperature and maintained during the reaction. The products were analyzed by using a HP 7890 gas chromatograph (GC) equipped with a SE-54 capillary column ($60 \text{ m} \times 0.25 \text{ mm} \times 0.25 \mu\text{m}$) connected to a flame ionization detector, and all the products were further confirmed by HP 7890A/5975C GC-MS. In order to calculate the carbon balance, the DME in gas phase was also analyzed and the amount of which was lower than 1% (not exhibited), while no CO and CO_2 were detected, because the contents of which must below the detection limits of the TCD. Also, formaldehyde (FA) in the liquid was determined using titration by sodium sulfite method. Meanwhile, tetrahydrofuran was used as the internal standard, the trioxane conversion (X_{TRI}), methanol conversion (X_{MeOH}), and the product selectivity, e.g., DMM_n selectivity (S_{DMM_n}) were calculated based on the total carbon atom numbers that converted (including methanol and trioxane), as given below.

$$X_{\text{TRI}} = \frac{(m_{\text{TRI}})_{\text{in feed}} - (m_{\text{TRI}})_{\text{in product}}}{(m_{\text{TRI}})_{\text{in feed}}} \times 100\% \quad (1)$$

$$X_{\text{MeOH}} = \frac{(m_{\text{MeOH}})_{\text{in feed}} - (m_{\text{MeOH}})_{\text{in product}}}{(m_{\text{MeOH}})_{\text{in feed}}} \times 100\% \quad (2)$$

$$S_{\text{DMM}_n} = \frac{(n+2) \times (m_{\text{DMM}_n})_{\text{in product}}}{(30n+46) \times [3(m_{\text{TRI}})_{\text{in feed}} \times X_{\text{TRI}}\%/90 + (m_{\text{MeOH}}\%/32)]} \times 100\% \quad (3)$$

3. Results and discussions

3.1. Structural features of the catalysts

Table 1 lists the physical properties of the $\text{SO}_4^{2-}/\text{Fe}_2\text{O}_3\text{-SiO}_2$ solid acids. The sulfur contents of the solid acids were obviously different, and the value (SO_3 was expressed in units) changed in the range of 2.9% and 6.8% that were prepared by the same equilibrium adsorption method. This is a typical problem of sulfated oxide solid acids that remains unsolved, partly due to the consecutive decomposition of the sulfur species that calcined at the temperature higher than 673 K (Supplementary data, Table SI 1), which is consistent with the sulfated titania as previously reported [24]. Also, the low reproducibility of the sulfated zirconia was observed under the similar preparation conditions [25]. Therefore, the catalysts used in this paper were taken from the same batches, in order to insure the reality of following experiments.

Fig. 1 shows the N_2 adsorption–desorption isotherms and the pore-size distribution curves of the catalysts. The S/Fe showed a typical IV isotherm pattern and exhibited a hysteresis loop starting from the relative pressure (P/P_0) at 0.7, and the value decreased to 0.4 for the S/Fe-Si-2 sample. Also, the silica doping increased the surface area, and reduced the pore volume and pore diameter of the sulfated iron oxides (Table 1). The S/Fe-Si-2 exhibited a narrow pore size distribution curve with the pore size of about 4.3 nm, while the S/Fe-Si-1 showed a wide pore size distribution from 4.3 nm to 20 nm. As for the S-Fe-HT sample, the average pore size obtained from the BJH method was 25.7 nm, which was not observed on the pore-size distribution curve (Fig. 1), it might be concluded that the pores of S-Fe-HT probably caused by the randomly packed particles.

Fig. 2 shows the SEM images of the samples. It must be accepted that the particle size and crystallinity degree of the catalysts are affected by preparation methods. In brief, all of the samples had no specific shapes and were accumulated by small particles. The elemental compositions of the samples by EDX spectra of selected area were exhibited in each photo, correspondingly, which are commonly in accordance with the results of XRF analyses (Table 1). Nevertheless, the Fe_2O_3 content of S/Fe-Si-2 was lower than that detected by EDX analysis, which might be caused by SiO_2 encapsulation and the depth limitation of this detection technique. As illustrated in Fig. 3, the diffraction peaks of S/Fe and S/Fe-HT sample were straight forwardly assigned to the $\alpha\text{-Fe}_2\text{O}_3$ crystalline structure (PDF # 33-0664) without any diffraction line of sulfate species, and the sharp diffraction peaks of S/Fe-HT indicated a larger crystalline size. By adding silica to the catalyst, the much weaker and broader peaks of S/Fe-Si-1 indicated the amorphous structure. Although the diffraction lines of S/Fe-Si-2 were not obvious, the peaks at 21.9° and 36.0° that attributed to (1 0 1) and (2 0 0) planes of SiO_2 appeared, respectively, indicating the aggregation of silica phase (PDF # 51-1379). That is, Fe_2O_3 can be homogenized mixed with silica, thicker film of SiO_2 formed when the Fe/Si molar ratio decrease to 0.36, and these results are consistent with SEM-EDX analyses. Also, the average crystallite sizes of S/Fe and S/Fe-HT were

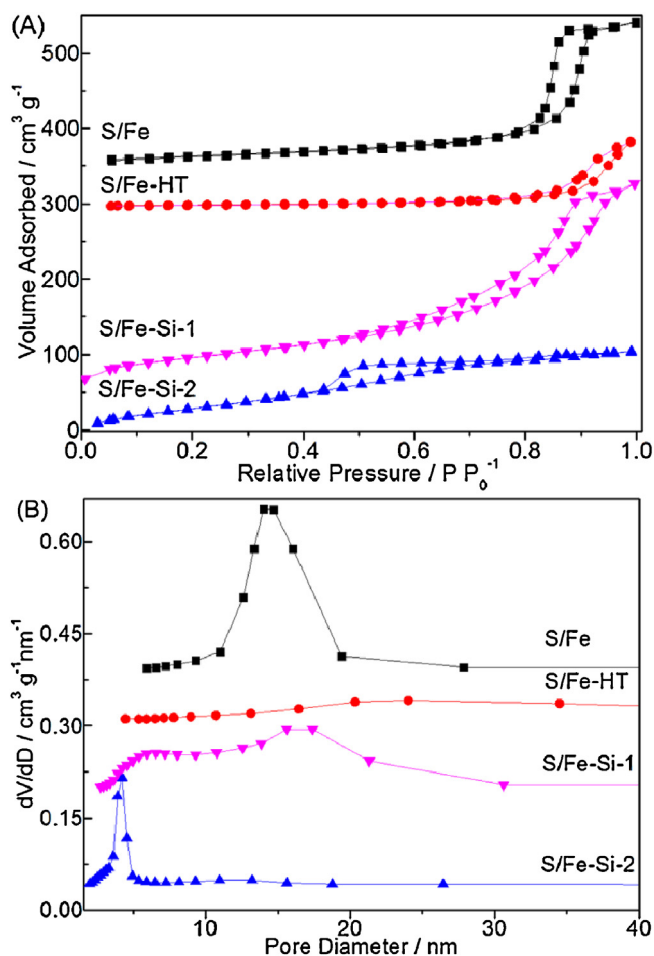


Fig. 1. (A) N_2 adsorption–desorption isotherms and (B) the corresponding BJH pore-size distribution curves of the catalysts.

about 15 nm and 38 nm, respectively, which were calculated from the half-width of (104) line of $\alpha\text{-Fe}_2\text{O}_3$ phase ($2\theta = 33.1^\circ$), according to the Scherrer's equation [26]. Accordingly, the surface areas of S/Fe and S/Fe-HT were only $72 \text{ m}^2 \text{ g}^{-1}$ and $26 \text{ m}^2 \text{ g}^{-1}$ due to the large crystalline size, respectively, which were much smaller than silica-doped samples (about $200 \text{ m}^2 \text{ g}^{-1}$). This is because it might have interactions between iron oxide and SiO_2 matrix by the formation of Fe–O–Si bonds, which helps to hinder the particle growth of iron oxide, and thus have higher surface areas [27].

Three types of sulfate species have been reported on the surface of sulfated oxides, including the classical sulfate, pyrosulfate and thionyl tetraoxide species, which can be distinguished from the simple H_2 -TPR-MS technique [28–30]. As shown in Fig. 4, there were only two types of products, H_2O and SO_2 were detected, accompanied by H_2 consumption, and no H_2S was emitted over all the samples during the H_2 -TPR-MS process. Meanwhile, only

Table 1
The physical properties of the catalysts.

Catalyst	S_{BET}^a	V_p^a	d_p^a	Compound formula, wt% ^b			Compound formula, wt% ^c		
	$\text{m}^2 \text{ g}^{-1}$	$\text{m}^3 \text{ g}^{-1}$	nm	SO_3	Fe_2O_3	SiO_2	SO_3	Fe_2O_3	SiO_2
S/Fe	74	0.32	13.5	6.8	93.2	–	6.5	93.5	–
S/Fe-HT	26	0.15	25.7	5.2	94.8	–	5.1	94.9	–
S/Fe-Si-1	205	0.46	9.6	6.8	63.6	29.6	6.3	63.7	30.0
S/Fe-Si-2	206	0.22	4.3	2.9	31.3	65.8	2.6	20.2	77.2

^a S_{BET} : specific surface area calculated by the BET method, V_p (pore volume) and d_p (pore size) obtained from the adsorption isotherm by the BJH method.

^b Based on XRF analyses.

^c Detected by SEM-EDX.

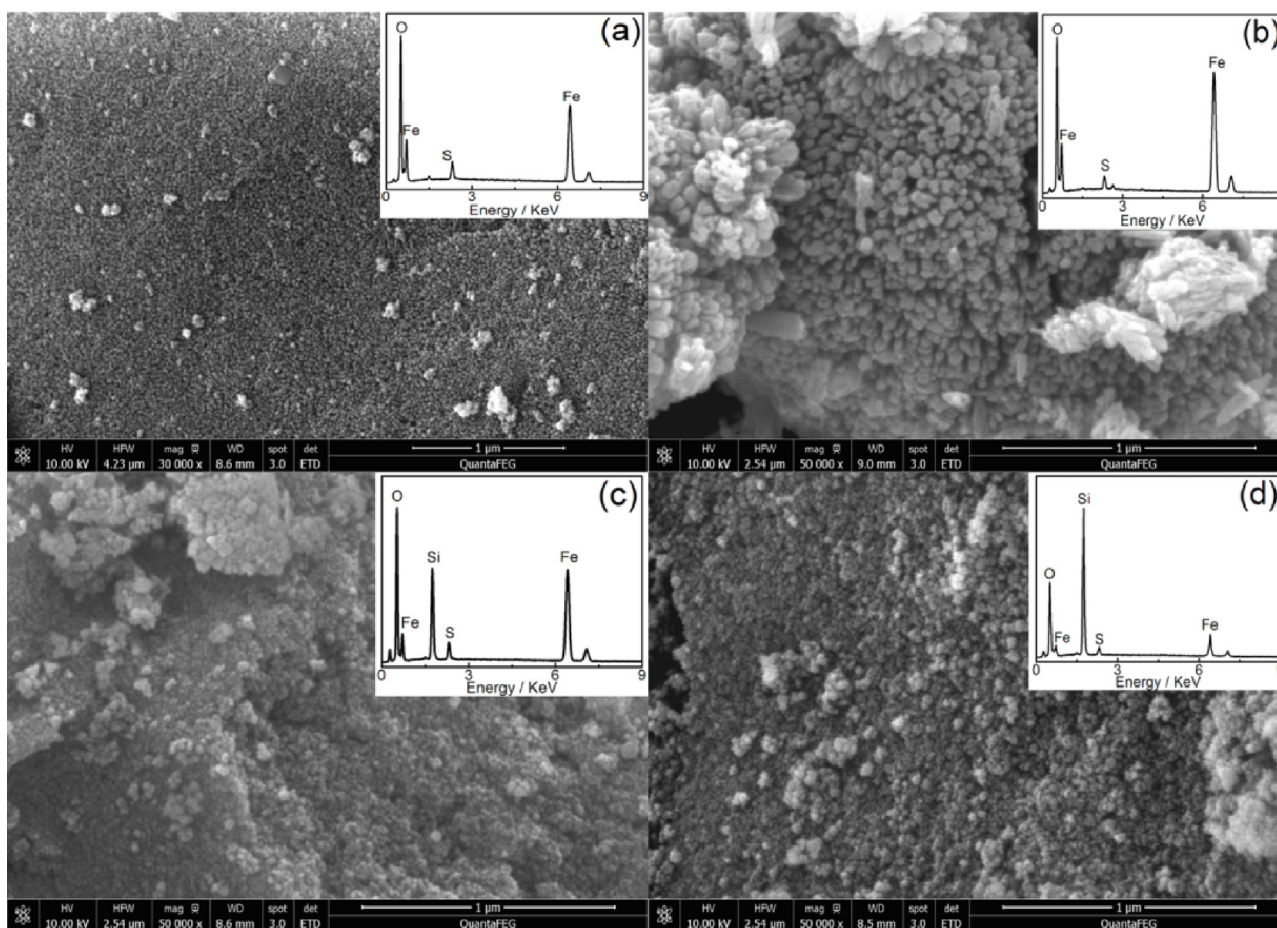


Fig. 2. SEM images of the S/Fe (a), S/Fe-HT (b), S/Fe-Si-1 (c), S/Fe-Si-2 (d); and the EDX spectra of selected areas, correspondingly.

SO₂ emitted and no other sulfur-containing product evolved at increased temperatures. Based on this, it can be concluded that there are only pyrosulfate species ($-\text{SO}_2-\text{O}-\text{SO}_2-$) on all the present catalysts as reported [28,31], because these species are not much bonded to the surface and should be readily reduced to SO₂. Meanwhile, Fe₂O₃ showed two hydrogen consumption peaks appearing at 623 K and 893 K (Fig. SI 1), which represented the reduction of Fe₂O₃ to Fe₃O₄/FeO (and finally to FeO) and FeO to Fe,

respectively [32]. This is because the reduction peak of Fe₂O₃ to FeO is close to the reduction temperature of Fe₂O₃ to Fe₃O₄. The simple sulfur species (SO₂) emission must be attributed to the homogeneity of sulfate species on all the four sulfated oxides, in other words, they have the same acid sites that undoubtedly generated by sulfur promotion. In brief, the low temperature reduction peaks of sulfated samples are slightly higher than the bare iron oxide. And, the S/Fe showed two overlapped hydrogen consumption peaks at 660 K and 698 K, while the other samples had only one reduction peak, indicating that the sulfate species should hinder the reduction behaviors of iron oxide to a certain extent. In relation to this issue, the higher the reduction temperature, the stronger the interaction between iron atoms and sulfate species, which would seem to imply that there exist much stronger interactions between iron metal and S=O bonds for the S/Fe sample, inevitably. Further, this stronger interaction should lead to the stronger acid strength on the sulfated oxides [22].

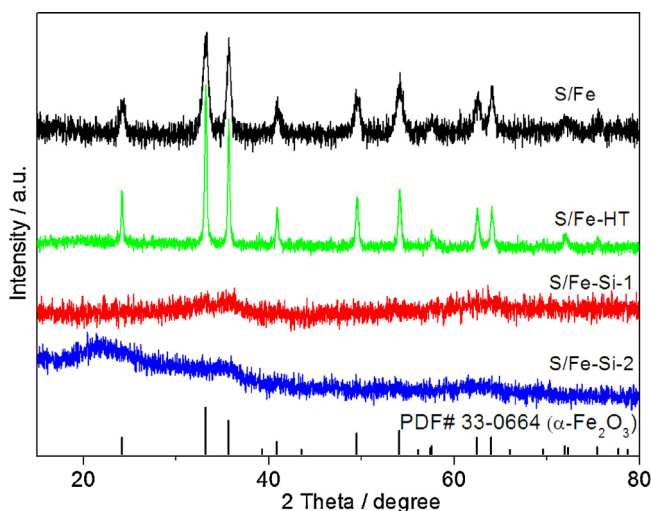


Fig. 3. XRD patterns of the catalysts.

3.2. Acid strength distribution and acidic properties

As shown in Fig. 5, NH₃-TPD profiles were carried out to evaluate the acidic properties of the samples. All the sulfated oxides had obviously two peaks at about 431 K and 679 K, corresponding to NH₃ desorbed from the weak and medium strong acid sites, respectively, the total amounts of which must including the sum of Brønsted and Lewis acid sites [25,33]. Compared to the silica doped samples, the total number of acid sites on S/Fe-HT and S/Fe were lower, which were 41 μmol g⁻¹ and 114 μmol g⁻¹, respectively, probably due to the lower surface areas [34]. As for bare

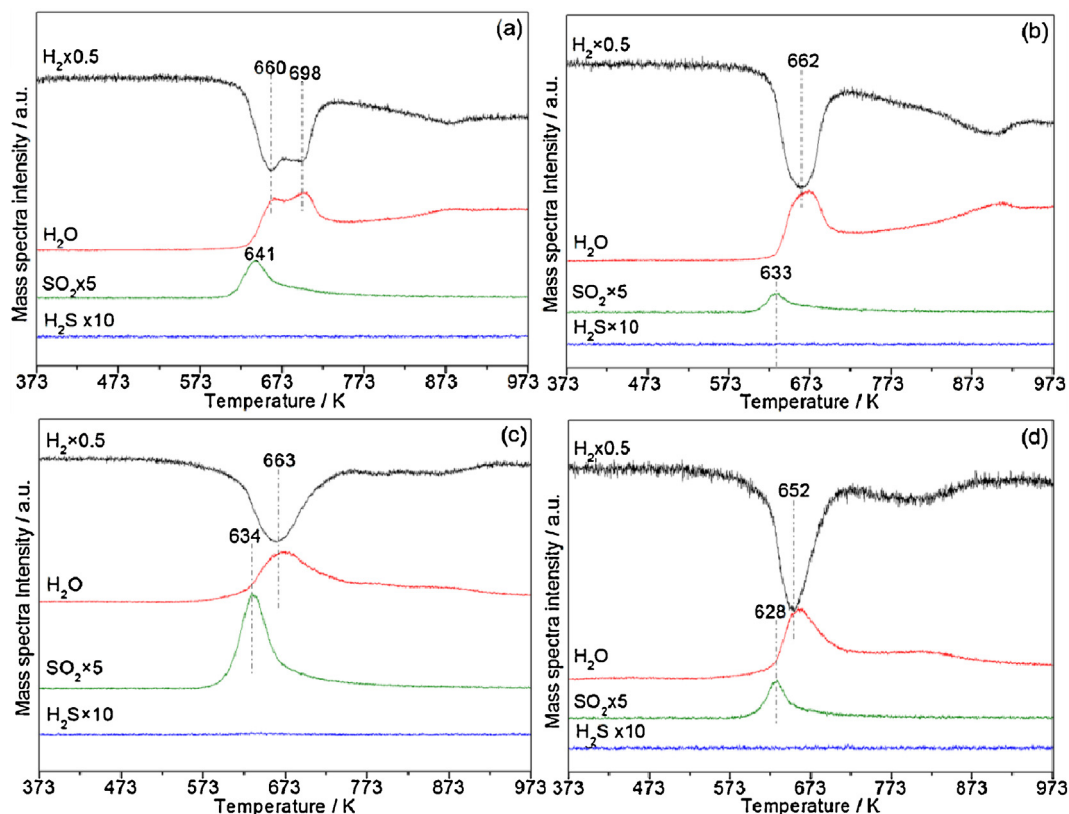


Fig. 4. Products evolution over the S/Fe catalyst during H_2 -TPR that recorded by mass spectrometry: (a) S/Fe, (b) S/Fe-HT, (c) S/Fe-Si-1, (d) S/Fe-Si-2.

Fe_2O_3 , there was almost no ammonia desorbed due to its basic nature (Fig. SI 2). For instance, there are also no ammonia and pyridine adsorption peaks for MgO and SiO_2 , because they have no acid sites [35]. From this point of view, it is obviously that the acid properties of the present catalyst are originated from sulfur promotion. However, the catalysts without silica have higher acid densities and higher fraction of medium strong acids, and thus show better catalytic activities, e.g., the higher DMM₂₋₈ formation rate as discussed in Section 3.4.

As observed in Fig. 6, in situ DRIFTS spectra were recorded after pyridine adsorbed and degassed at 423 K, while the physisorbed pyridine had been removed [36]. It is well known that the band at 1540 cm^{-1} and 1639 cm^{-1} correspond to pyridine adsorbed on the Brønsted acid sites (BPY), while the band at 1450 cm^{-1} and

1611 cm^{-1} are ascribed to pyridine adsorbed on Lewis acid sites (LPY), and the peak around 1490 cm^{-1} is due to the overlapping vibrations of both BPY and LPY [35,36]. For S/Fe and S/Fe-HT catalysts, the intensity of the peaks assigned to BPY is much higher than that of LPY. By the addition of silica to iron oxide, the bands at 1540 cm^{-1} and 1489 cm^{-1} reduced, while the band at 1450 cm^{-1} increased, indicating the number of Lewis acid sites increased, which is further confirmed by the number of Brønsted and Lewis acid sites (Table 2). Furthermore, the asymmetric stretching frequency of the S=O bond is related to the acidic sites on sulfated oxides, because the superacidic property is attributable to the

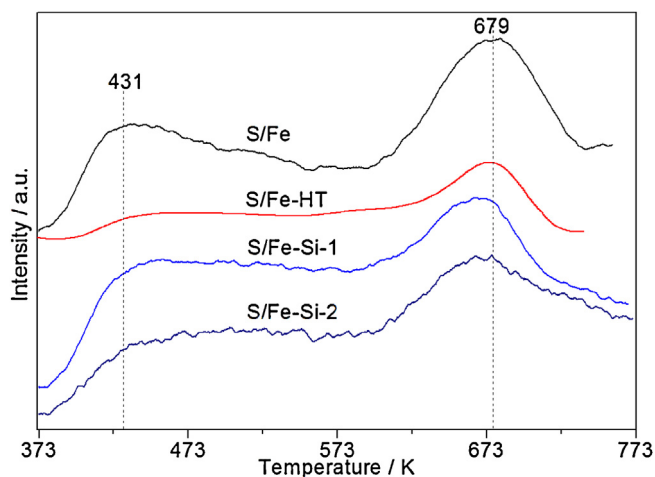


Fig. 5. NH_3 -TPD profiles of the catalysts.

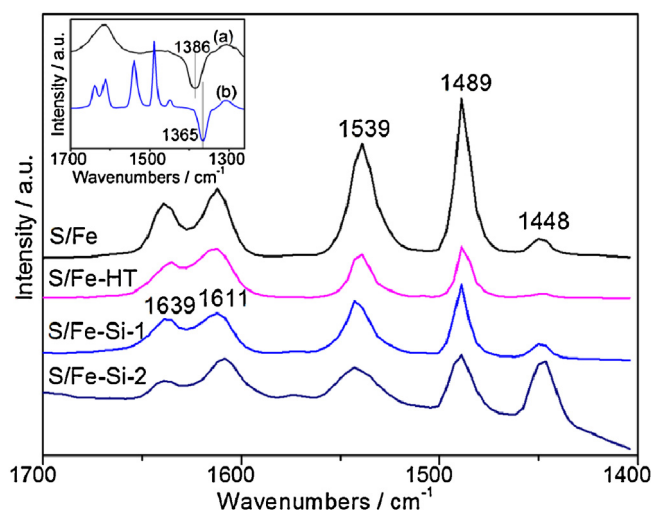


Fig. 6. IR spectra of pyridine adsorbed on all the catalysts, and the typical IR spectra of S/Fe catalyst (inset): (a) evacuated at 673 K, (b) after pyridine adsorbed and evacuated at 423 K.

Table 2

Surface acid distributions of the catalysts.

Catalyst	Amount of acid sites, $\mu\text{mol g}^{-1}$					Brönsted acid fraction, % ^b	Acid density, $\mu\text{mol m}^{-2}$
	Total ^a	Weak ^a	Medium strong ^a	Brönsted ^b	Lewis ^b		
S/Fe	114	50	64	99	15	87	1.58
S/Fe-HT	41	15	26	37	4	91	1.57
S/Fe-Si-1	178	87	91	132	46	74	0.87
S/Fe-Si-2	129	77	52	35	94	27	0.63

^a Determined by NH_3 -TPD profiles.^b Calculated based on pyridine adsorption.

double-bond nature of the $\text{S}=\text{O}$ bond that formed by the interaction between sulfate species and oxides [22,37,38]. The bond order was calculated from an empirical equation (n , in Eq. (4)), in order to elucidate the interaction between the adsorbed pyridine molecules and surface sulfate species. Where ν_{asym} represents the wavenumber of asymmetric stretching frequency of SO double bond, and the bond order changes (ΔB) before and after pyridine adsorption reflects the acid strength of sulfated oxides [22].

$$n = 6.9741 \times 10^{-7} \left(\frac{9 \times \nu_{\text{asym}}}{10} + 40 \right)^2 + 0.7 \quad (4)$$

As seen from the IR spectra of the typical S/Fe catalyst (Fig. 6, inset), the asymmetric $\text{S}=\text{O}$ stretching frequency shifted from 1386 cm^{-1} to a much lower frequency (1365 cm^{-1}) after pyridine adsorption, corresponding to a change of 0.034 in the bond order (the others, listed in Table 3). Therefore, the surface sulfur complex has a strong tendency to reduce its bond order by the adsorption of basic molecules such as pyridine, which is directly related to the acid strength of sulfated oxides. It is clear that the change in bond order by pyridine adsorption is highest in S/Fe catalyst, which must have the strongest acid strength. The ΔB of S/Fe-HT is lower than S/Fe catalyst, probably because of the higher crystallinity of iron oxide (the crystallization extent was 72.9%) that lead to a weaker interaction with sulfate species. The silica-doped sample (S/Fe-Si-2) has the lowest ΔB value, which is consistent with the report that sulfate species have no promoting effect on SiO_2 , and thus cannot generate strong acidity [22]. However, the amounts of Lewis acids are evidently increased, while the Brönsted/Lewis acid ratio decreased by introducing SiO_2 into S/Fe catalysts.

3.3. Methanol/trioxane adsorption and desorption

In situ DRIFTS spectra of CH_3OH adsorbed on all the catalysts are illustrated in Fig. 7. At 323 K, when methanol adsorbed on the S/Fe sample (Fig. 7a), two bands at about 2950 cm^{-1} , 2856 cm^{-1} , and three bands at 1012 , 1034 and 1053 cm^{-1} were due to the antisymmetric and symmetric stretching vibrations of CH_3 and stretching vibrations of $\text{C}-\text{O}$, respectively. Simultaneously, the band at 1451 cm^{-1} was ascribed to deformation mode of CH_3 , all of which represented the adsorbed methoxy species that resulting from $\text{CH}_3\text{O}-\text{H}$ dissociation on the catalyst surface

[39,40]. Meanwhile, the band at 1356 cm^{-1} that belong to formate species appeared at the same time, owing to the further oxidation of methoxy species [40]. The OH stretching vibration bands located between 3700 and 3600 cm^{-1} , while the H_2O deformation vibration was observed at 1642 cm^{-1} [34]. After evacuation at 323 K, all the intensity of the bands belong to $\nu(\text{C}-\text{O})$ and $\delta(\text{CH}_3)$ decreased, due to desorption of the physically adsorbed surface species. The band intensity of formate species increased at the same time, which began to decrease at temperatures higher than 473 K, i.e., they might convert to carbonate species, progressively. Furthermore, the bands at 2950 , 2856 , and 1012 cm^{-1} decreased at elevated temperatures, and finally disappeared at 573 K, it might be due to the further oxidation of methoxy species and the reaction of methoxy species with formate species that formed, subsequently.

Further, when methanol was adsorbed and degassed, and then CH_2O (trioxane dissociation) was adsorbed on the S/Fe sample at 323 K (Fig. SI 3), and the methoxy species disappeared at a much lower temperature (323 K), because of the direct reaction of methoxy species with CH_2O species, while the evolution tendency of adsorbed species were the same with CH_3OH adsorbed on S/Fe, at elevated temperatures. Most likely, the adsorbed methoxy species underwent dehydrogenation to CH_2O species, which could be further converted to formate or methylformate species. When CH_3OH adsorbed on S/Fe-Si-1 and S/Fe-Si-2, the IR bands at 3740 or 3745 cm^{-1} that assigned to medium strong Lewis acid sites were appeared [34]. Because the silica incorporated catalyst has a higher fraction of Lewis acid sites, which is in agreement with the pyridine adsorption results (Fig. 6 and Table 2). The evolution of surface species on the silica-doped catalysts was similar to the other catalysts, including the bare Fe_2O_3 sample (Fig. SI 4). The main difference is the desorption temperature of the surface methoxy species, which totally disappear on the S/Fe and S/Fe-HT catalysts at 573 K, and these species still remain on the surface of the others at 673 K. It must be admitted that the strong adsorption is unfavorable to the present condensation reaction (Table 3 and Fig. 9). Indeed, HCOOCH_3 and DME were also detected by GC analyses in the products, probably due to the further reaction between formate and methoxy species and dehydration of methoxy species, respectively. In all, the IR spectra demonstrate that the methoxy species formed immediately upon methanol adsorbed on the

Table 3Changes in bond order of SO structure and the specific reaction rate.

Catalyst	SO freq. ^a		Bond order ^b			TOF, h^{-1}c			
	Before	After	Before	After	$\Delta B \times 10$	MeOH	TRI	DMM ₂₋₈	MeOH/TRI
S/Fe	1386	1365	1.856	1.822	0.34	316	234	350	1.3
S/Fe-HT	1370	1356	1.830	1.802	0.28	429	79	103	5.4
S/Fe-Si-1	1375	1358	1.838	1.811	0.27	304	88	87	3.4
S/Fe-Si-2	1363	1354	1.819	1.805	0.14	360	56	5	6.4

^a The $\text{S}=\text{O}$ asymmetric stretching frequency before and after pyridine adsorbed (cm^{-1}).^b Bond order was calculated by the equation supported by Jin et al. [22], and ΔB represent the changes of $\text{S}=\text{O}$ bond order before and after pyridine adsorbed.^c TOF (turn over frequency) of trioxane (TRI) and methanol (MeOH), and the total carbon atom numbers that converted to DMM₂₋₈ per sulfur atom per hour (h^{-1}); MeOH/TRI was the TOF ratio of methanol and trioxane.

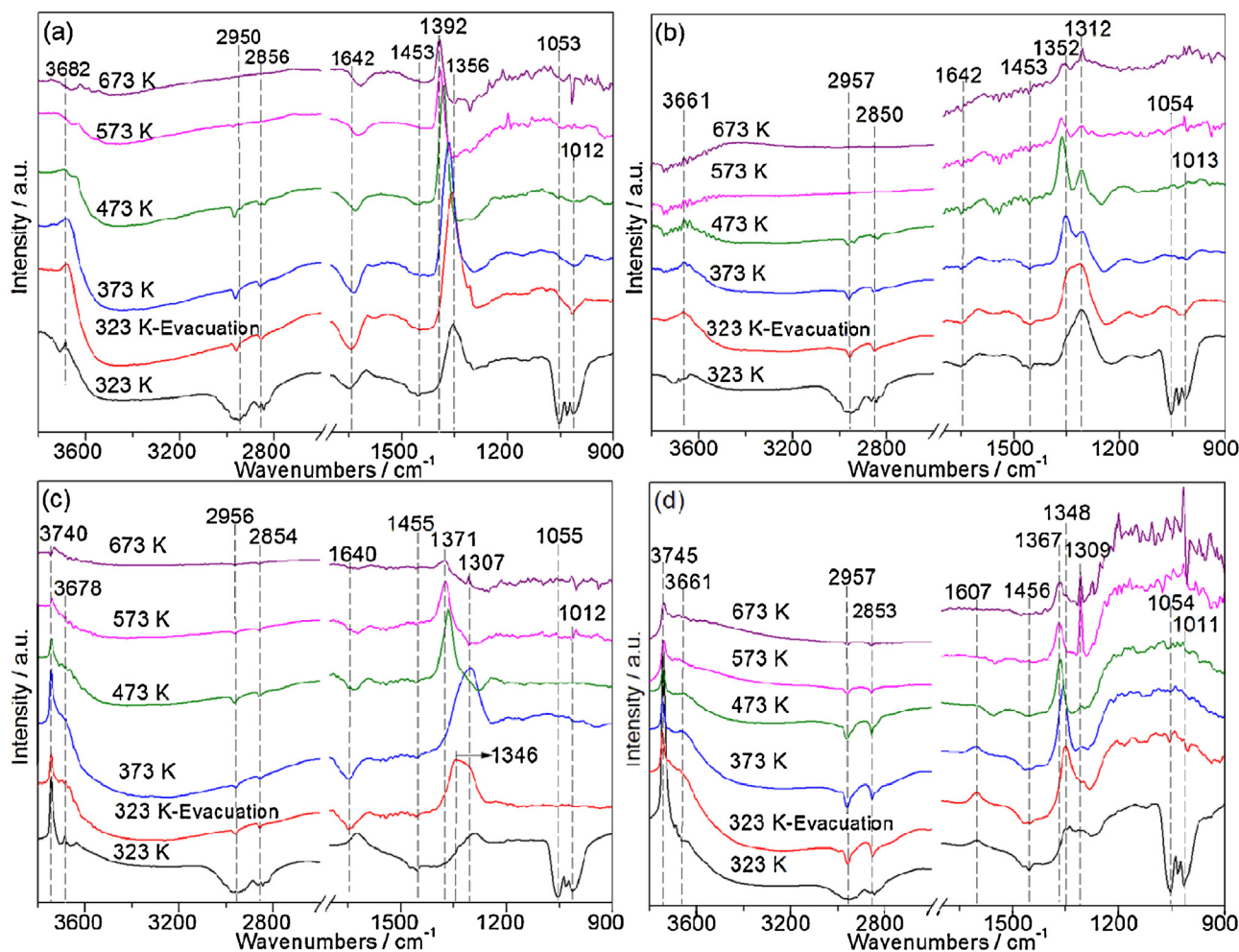


Fig. 7. DRIFTS spectra of CH_3OH adsorbed on the catalysts: (a) S/Fe, (b) S/Fe-HT, (c) S/Fe-Si-1, (d) S/Fe-Si-2.

catalyst, which are further oxidized into formate species through formaldehyde.

Compared to IR spectra of the adsorbed species, the desorbed species were also detected by MS, in order to reveal the methanol evolution behavior on the catalysts. Fig. 8 shows the TPD profiles of methanol adsorbed on the catalysts. For example, on the S/Fe catalyst, the desorption peak of CH_3OH was observed at 402 K, while two desorption peaks of CH_2O appeared at 402 K and 540 K, indicating the two adsorption sites on the catalyst surface. Because CH_2O was produced by dehydrogenation of the adsorbed methoxy species, which was consistent with the two different acid strength on the catalyst as have been illustrated by NH_3 -TPD profiles. CH_3OCH_3 started to evolve below 400 K, reached a maximum value at about 453 K, and remained in the products at temperatures as high as 573 K, which is formed by the dehydration of two adjacent methoxy species on the acid sites [34]. Simultaneously, there were mainly two desorption peaks of CO and CO_2 at about 400 and 553 K, indicative of the decomposition of methoxy species (including DME) and formate, respectively. Also, the high temperature desorption peak of CO_2 at about 773 K should be ascribed to the further oxidation of the methoxy related species that strongly adsorbed on the catalyst surface, e.g., formate and/or carbonate species remained on the catalyst at 673 K, as observed from IR spectra (Fig. 7). Expectedly, SO_2 was detected at the temperature above 570 K, which should be ascribed to the decomposition of sulfate species on the S/Fe catalyst. This phenomenon is also consistent with H_2 -TPR-MS results (Fig. 4), because sulfate species decompose at much lower temperatures under the reducing atmosphere,

which decompose obviously at temperatures higher than 773 K, when calcined in the air (Table SI 1).

Unfortunately, no DMM was detected in all the above experiments. Because of this, the DMM-desorption tests were also carried out, in order to reveal the reasons of present results (Fig. SI 5). After DMM adsorbed on the catalysts, desorption products were also followed the similar profiles with CH_3OH -TPD and no DMM were detected. Comparing with the methanol-TPD profiles, the CH_3OH and CH_2O desorption started to evolve at lower temperatures, especially, the desorption peak decreased from 402 K to 375 K on the S/Fe catalyst, indicative of the easier decomposition of DMM when adsorbed on the catalyst surface. More interestingly, the DME desorbed at almost the same temperature (Fig. 7 and Fig. SI 5), thus, it could be concluded that DMM is readily decomposed to CH_3OH and CH_2O , and the DME might be formed by dehydration of methanol on the catalyst surface, subsequently. At least, even if DMM species formed on the catalyst surface, they might decompose completely even at lower temperatures, and thus could not be detected by MS. Furthermore, on the Fe_2O_3 sample, owing to its basic nature, CO and CO_2 were almost the only desorption products and no DME was detected, which were accompanied by a small amounts of CH_2O , probably due to the DMM decomposition or oxidation during the TPD process (Fig. SI 6). Therefore, it must be pointed out again that all the IR spectra and TPD profiles of CH_3OH /DMM on the sulfated oxides (solid acids) are consistent with the S/Fe catalyst, indicating they have the same adsorption sites, essentially, the same active sites (generated by a iron atom and a sulfate ion) for methanol and trioxane condensation reaction.

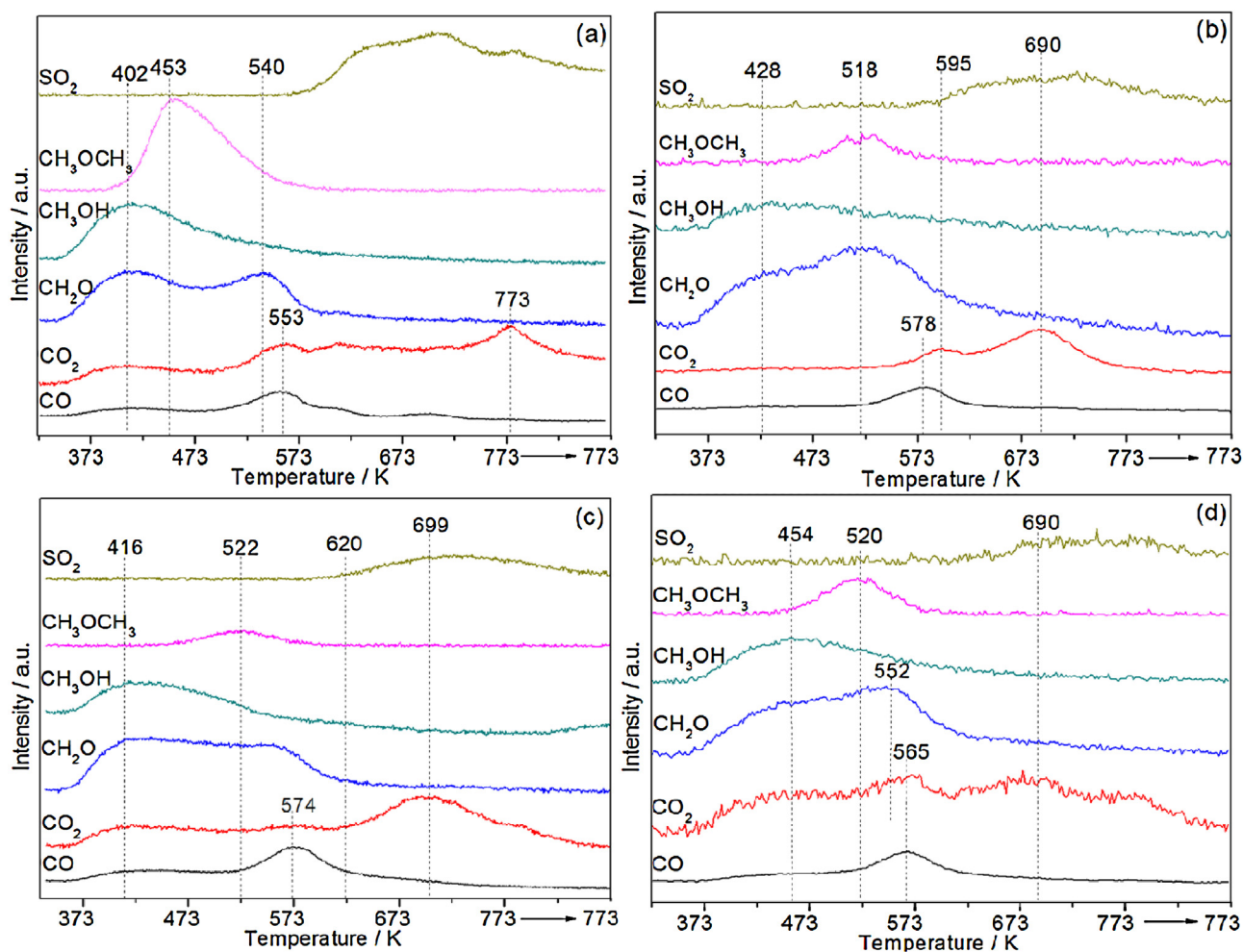


Fig. 8. TPD profiles of methanol adsorbed on the catalysts: (a) S/Fe, (b) S/Fe-HT, (c) S/Fe-Si-1, (d) S/Fe-Si-2.

Although the IR and TPD characterizations were carried out under vapor phase, the results could reveal some useful features for the liquid phase. As revealed by IR and TPD analyses, methoxy, CH_3OCH_3 and formate species are readily formed upon methanol and DMM adsorption on the catalysts. Further, the formation of oxidation products, especially methyl formate in the liquid phase (CO and CO_2 were not detected), implying the reduction of iron oxide that must weaken the bond strength between iron atoms and sulfate ions, unavoidably. This phenomena lead to the decomposition of sulfate species and thus the catalytic activity is decreased, and it should be accepted that the sulfur loss is a common problem that remains unsolved for sulfated oxide solid acids [17,41].

3.4. Catalytic performance and reaction pathway

On the S/Fe catalyst, the conversion of methanol and trioxane were 74.8% and 81.9%, respectively, and the DMM_{2-8} selectivity was 34.4%, which showed the highest activity among all the present catalysts (Table 4). On S/Fe-HT catalyst, the trioxane conversion was lower than S/Fe-Si-1, while the DMM_{2-8} selectivity was slightly reversed. The S/Fe-Si-2 had the lowest catalytic activity, the conversion of methanol and trioxane were 35.8% and 8.3%, respectively, and DMM_2 selectivity was only 0.9%, while no product of DMM_n ($n > 2$) was detected. The DME in gas phase was also analyzed and the amount of which was lower than 1% (not exhibited). In addition, the highest formaldehyde selectivity of 35.2% was obtained over the S/Fe catalyst, which must imply the importance of trioxane

dissociation rate during DMM_n synthesis as compared to the other samples, and the catalyst showed a relatively good recycle performance in our recently published paper (shown in Fig. SI 7) [17].

In addition, as seen from the average pore size of the catalysts (Table 1 and Fig. 1), the methanol/trioxane conversion rate and/or the products formation rate are not affected by the pore sizes of the catalysts, implying that the inner pore diffusion is not likely limiting the intrinsic rates. Typically, the specific reaction rates on S/Fe-HT and S/Fe-Si-1 are similar, although their pore sizes differ significantly, suggesting that the internal mass diffusion on these catalysts has little effect on methanol/trioxane conversion rate and products selectivity. The present results are in good accordance with the report that it dose not indicate a dependence of glycerol turnover rate on the pore sizes of varied solid acids [42]. Also, the acid density does not essentially affect the reaction activity (Table SI 2, Fig. SI 7). However, the higher acid density of the present catalysts to a certain extent, the higher catalytic activity, e.g., the DMM_{2-8} formation rate, because the higher acid density should facilitate further condensation reaction between the adsorbed species on the catalysts surfaces. That is, the acid properties of the catalyst play a determining role for the ring-opening and condensation reaction of trioxane with methanol. It is more convincing to compare the reaction performances by considering the number of active sites (sulfur species), as illustrated in Fig. 9. Higher Brönsted/Lewis acid site (B/L) ratio facilitate the methanol conversion, while the specific reaction rate of trioxane and formaldehyde, methyl formate and DMM_{2-8} production rate per sulfur atom follow the same changing

Table 4Catalytic activity and DMM_n products distributions for the condensation of methanol and trioxane over the catalysts.

Catalyst	Conversion, % ^a		Selectivity of the products, C _{mol} , % ^b										
	MeOH	TRI	FA	MF	1	2	3	4	5	6	7	8	2–8
S/Fe	74.8	81.9	35.2	2.7	24.7	11.2	8.6	5.1	2.9	1.5	0.6	0.2	34.4
S/Fe-HT	78.0	21.3	15.4	0.8	67.3	12.6	2.4	0.4	–	–	–	–	15.4
S/Fe-Si-1	71.6	30.9	20.7	2.1	53.1	11.4	3.0	0.6	0.1	–	–	–	15.2
S/Fe-Si-2	35.8	8.3	11.7	0.4	76.1	0.9	–	–	–	–	–	–	0.9

^a MeOH, methanol, TRi, trioxane.^b FA, formaldehyde, MF, methylformate, and 1–8 denotes the DMM_n ($n = 1–8$), respectively. Reaction conditions: 403 K, 2 h, $n_{\text{MeOH}}/n_{\text{TRi}} = 1.5$ (molar ratio), catalyst amount, 1.5% (mass ratio).

tendency, all of which show a maximum, and then decrease when the B/L ratio is increased (Fig. 9A). Further, as seen from Fig. 9B, the TOF (turn over frequency) value of methanol over the S/Fe catalyst is slightly lower than S/Fe-HT sample. There are probably two reasons for this phenomenon. Firstly, in relation to the reaction equilibrium, the higher CH₂O concentration in the reaction liquid might inhibit the methanol conversion to CH₂O, and CH₂O mainly produced by trioxane dissociation. Secondly, methanol could be readily converted to CH₂O and related products on the acid sites of the present catalysts, i.e., the acid strength (ΔB) of all the four catalysts is sufficient for methanol conversion, which have been proved by IR and TPD techniques. Correspondingly, the S/Fe with the highest ΔB value that showed the highest TOF value of trioxane, formaldehyde, methyl formate and DMM_{2–8}, which are in accordance with the magnitude of S=O stretching frequency shifts, essentially, the

acid strength of the catalyst obviously. Therefore, ΔB is directly related to the catalytic activities, which is in good agreement with the results obtained by other research groups [22,38].

Also, as shown in Table 3, the S/Fe with the methanol/trioxane specific reaction rate of 1.3 showed the best activity, which is quietly in accordance with the present raw material molar ratio of 1.5, and which cannot be coincidence, because we also found the best molar ratio of methanol/trioxane for DMM_n synthesize was 1.2, previously [17]. In all, this reaction is commonly considered to be a step-wise reaction, because the products with a higher polymerization degree usually have a poor yield [14,16,17,21,43]. Higher CH₂O production rate (on S/Fe catalyst) in the reaction systems favors the formation of DMM_n with higher chain length, which has been proved by the reaction results (Table 4). When the methanol conversion rate become more faster than trioxane decomposition rate, there are predominantly lower chain length products, e.g., mainly DMM and DMM₂ (include DME and other byproducts) formed on the S/Fe-Si-2 catalyst, especially. Accordingly, the specific reaction rate of trioxane and DMM_{2–8} are mainly controlled by the Brønsted acid sites on the SO₄^{2–}/Fe₂O₃ solid acids (Fig. SI 9). In fact, there may exist the synergistic effect between Brønsted and Lewis acid sites that is still unclear. The results are in good agreement with the report that anionic vacancies acting as Lewis acids, which were evidenced as the active sites for synthesis of DMM over FeMo mixed oxides, and no DMM_{2–8} were formed [6]. Recently, the sorption processes of reactants on the catalyst have been considered to be the rate determining steps, because the surface reactions are comparatively fast over the Amberlyst 46 catalyst, according to the adsorption-based model proposed by Burger et al. [19]. Herein, trioxane decomposition rate is well correlated with the acid strength of the catalysts and the reaction performance. Thus, it is reasonably to conclude that the trioxane decomposition process should be a vital step, depending on the present research and the published reports [2,14,16]. Certainly, the reaction performance is essentially controlled by the appropriate acid sites on the catalyst. The acid strength (ΔB) decreased and Lewis acid sites increased when silica are incorporated into the iron oxides and thus lead to a lower DMM_{2–8} production rate, accordingly. Therefore, these results indicate that the catalytic activity is determined by the acid strength, Brønsted acid sites of the catalysts, and are also influenced by the acid density and methanol/trioxane molar ratio in the raw material. Also, a large number of acid sites and a higher surface area of the catalyst facilitate the reactants adsorption process, and thus improve the overall reaction activities.

Indeed, the DMM_n products with the structure of CH₃O–(CH₂O)_n–CH₃ are synthesized by the acidic catalysts that must include the carbon chain growth and termination process. Methanol, DME ($n = 1$ in Eq. (8)) and DMM ($n = 2$ in Eq. (8)) take the role as the capping agent, while trioxane acts as the mainly carbon source for chain growth that are commonly recognized [2,14]. Because the IR spectra and TPD profiles of CH₃OH and DMM over all the catalysts follow the same adsorption-desorption

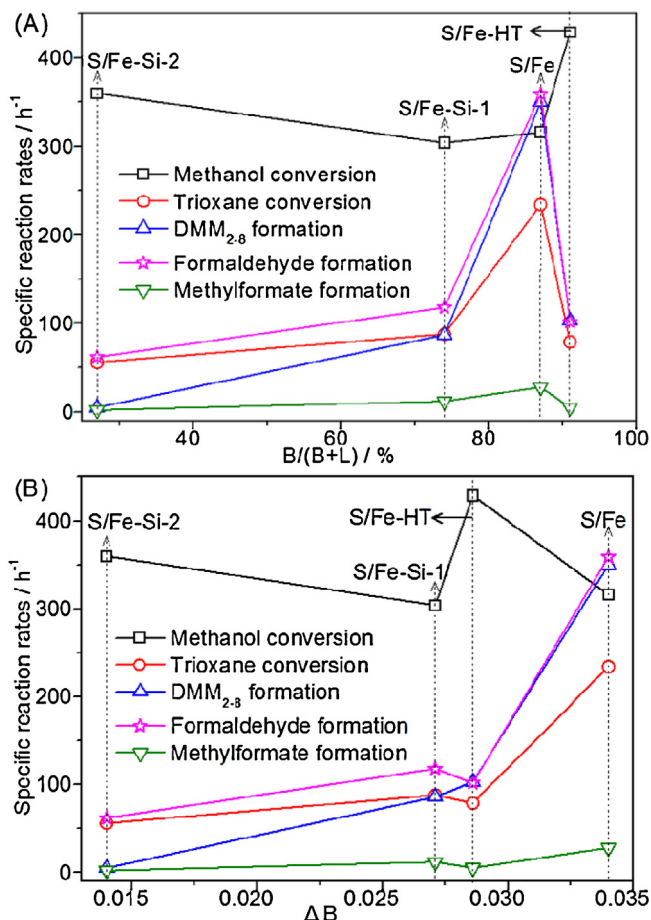
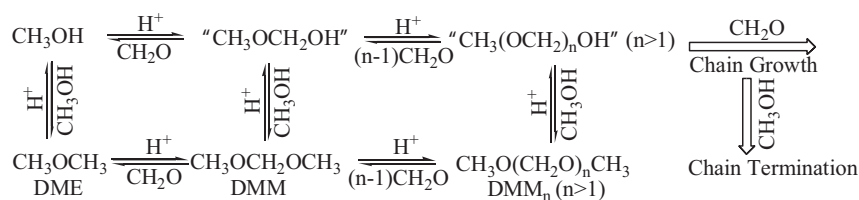
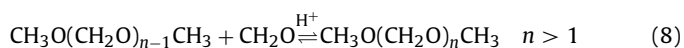
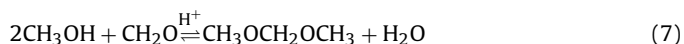


Fig. 9. Specific reaction rate per active sites (sulfur) against the Brønsted/Lewis acid sites (A), and acid strength (ΔB) of the catalysts (B).



Scheme 1. Proposed mainly pathways of methanol and trioxane condensation reaction.

behavior, it can be concluded that they have the similar reaction pathways in the reaction of methanol with trioxane. The reactions mainly involved are listed below:



The formation of CH_2O , DME and methyl formate have been proved by the activity tests, IR characterization and methanol/DMM-TPD techniques. Based on the above results, first trioxane is converted to CH_2O on the acid sites (Eq. (5)), and followed by the condensation reaction with methanol to obtain DMM_n products (Eqs. (7) and (8)), during which process methanol could form DME (Eq. (6)) over the acidic catalysts. When the dissociation rate of Eq. (5) is much lower than Eq. (6), e.g., there are probably more DME and DMM in the products. Therefore, the desired products with varied degree of polymerization are possibly regulated by the relative reaction rates of carbon chain growth and termination. From this point of view, the regulation of catalyst acid properties is the core technique, in order to monitor the reaction rate of the two critical processes.

The hemimethylals have been supposed to be the intermediates during DMM synthesis, although they are hardly detected by IR and TPD techniques in the adsorption and desorption processes because of their thermodynamic instability [8,39]. Indeed, $\text{CH}_3\text{OCH}_2\text{OH}$ species appear as the key intermediate which were detected by transient isotopic experiments in the methanol selective oxidation to DMM [44]. As is well known, the polyoxymethylene dimethyl ethers (DMM_n) themselves are polyoxymethylene acetals, which can be readily produced through polyoxymethylene hemiacetals ($\text{CH}_3(\text{OCH}_2)_n\text{OH}$) due to their more instabilities. Therefore, we can propose the reaction pathways for methanol/trioxane condensation reaction over the sulfated iron oxide as shown in Scheme 1. Briefly, the carbon chain growth when $\text{CH}_3(\text{OCH}_2)_n\text{OH}$ react with CH_2O , and then $\text{CH}_3(\text{OCH}_2)_{n+1}\text{OH}$ formed; while the chain termination occur when $\text{CH}_3(\text{OCH}_2)_n\text{OH}$ react with CH_3OH , and then the DMM_n products are finally produced on the appropriate acidic sites.

4. Conclusion

We report herein the physicochemical properties of model $\text{SO}_4^{2-}/\text{Fe}_2\text{O}_3\text{-SiO}_2$ catalysts with varied acid strength and Brønsted acid sites. These catalysts exhibited very different features for the reaction of methanol with trioxane, regardless of the activity and products distribution. Experimental results showed that the internal mass diffusion on these catalysts had no effect on this reaction activity. The S/Fe sample showed the best catalytic performance, and S/Fe-Si-2 with the highest number of Lewis acid sites led to the lowest catalytic activity. Based on the characterizations and activity tests, the present catalysts showed a similar reaction pathway. The carbon chain growth and termination rate are critical to the DMM_n

production, and trioxane dissociation process seems to be a vital step, meanwhile, polyoxymethylene hemiacetals are supposed to be the key intermediate species to synthesis DMM_n. In all, the catalytic activity and selectivity are determined by the acid strength, Brønsted acid sites of the catalysts, and are also influenced by the acid density and methanol/trioxane molar ratio in the raw material. While a large number of acid sites and a high surface area of the catalyst might facilitate the reactants adsorption, and thus promote the overall reaction activity.

Acknowledgments

The authors are grateful to the National Natural Science Foundation of China (NSFC, No. 21203220, 21133011), Jiangsu Planned Projects for Postdoctoral Research Funds of China (No. 1302070C), China Postdoctoral Science Foundation (No. 2014M551674) and the National Basic Research Program of China (973 Program, No. 2011CB201404) for financial support.

Appendix A. Supplementary data

Supplementary data associated with this article can be found, in the online version, at <http://dx.doi.org/10.1016/j.apcatb.2014.10.033>.

References

- [1] T.J. Bruno, T.M. Lovestead, J.R. Riggs, E.L. Jorgenson, M.L. Huber, *Energy Fuels* 25 (2011) 2493–2507.
- [2] J. Burger, M. Siegert, E. Ströfer, H. Hasse, *Fuel* 89 (2010) 3315–3319.
- [3] C. Arcoumanis, C. Bae, R. Crookes, E. Kinoshita, *Fuel* 87 (2008) 1014–1030.
- [4] K.D. Vertin, J.M. Ohi, D.W. Naegeli, K.H. Childress, G.P. Hagen, C.I. McCarthy, A.S. Cheng, R.W. Dibble, *SAE Papers*, 1999, 1999-01-1508.
- [5] R. Zhu, X. Wang, H. Miao, X. Yang, Z. Huang, *Fuel* 90 (2011) 1731–1737.
- [6] K.-A. Thavornprasert, M. Capron, L. Jalowiecki-Duhamel, O. Gardoll, M. Trentesaux, A.-S. Mamede, G. Fang, J. Faye, N. Touati, H. Vezin, J.-L. Dubois, J.-L. Couturier, F. Dumeignil, *Appl. Catal. B* 145 (2014) 126–135.
- [7] Y. Yuan, T. Shido, Y. Iwasawa, *Chem. Commun.* (2000) 1421–1422.
- [8] H. Liu, E. Iglesia, *J. Phys. Chem. B* 107 (2003) 10840–10847.
- [9] H. Zhao, S. Bennici, J. Shen, A. Auroux, *J. Catal.* 272 (2010) 176–189.
- [10] US Patent 20110288343A1 (2011).
- [11] US Patent 20100056830A1 (2010).
- [12] US Patent 6437195B2 (2002).
- [13] US Patent 20080221368 (2008).
- [14] Y. Zhao, Z. Xu, H. Chen, Y. Fu, J. Shen, *J. Energy Chem.* 22 (2013) 833–836.
- [15] Y. Lei, Q. Sun, Z. Chen, J. Shen, *Acta Chim. Sinica* 67 (2009) 767–772.
- [16] Q. Zhao, H. Wang, Z. Qin, Z. Wu, J. Wu, W. Fan, J. Wang, *J. Fuel Chem. Technol.* 39 (2011) 918–923.
- [17] F. Zhao, H. Li, H. Song, C. Xia, *Nat. Gas Chem. Ind.* 38 (2013) 1–6.
- [18] J. Burger, H. Hasse, *Chem. Eng. Sci.* 99 (2013) 118–126.
- [19] J. Burger, E. Ströfer, H. Hasse, *Ind. Eng. Chem. Res.* 51 (2012) 12751–12761.
- [20] J. Burger, E. Ströfer, H. Hasse, *Chem. Eng. Res. Des.* 91 (2013) 2648–2662.
- [21] M. Arvidsson, M.E. Fakley, M.S. Spencer, *J. Mol. Catal.* 41 (1987) 391–393.
- [22] T. Jin, T. Yamaguchi, K. Tanabe, *J. Phys. Chem.* 90 (1986) 4794–4796.
- [23] M.R. Basila, T.R. Kantner, *J. Phys. Chem.* 70 (1966) 1681–1682.
- [24] C.H. Zhu, M.C. Guo, X.B. Zhu, J.F. Chen, J.H. Su, *Appl. Magn. Reson.* 42 (2012) 313–320.
- [25] N. Katada, T. Tsubaki, M. Niwa, *Appl. Catal. A* 340 (2008) 76–86.
- [26] H.P. Klug, L.E. Alexander, *X-ray Diffraction Procedures*, John Wiley, New York, 1974, pp. 642.
- [27] M. Qing, Y. Yang, B. Wu, J. Xu, C. Zhang, P. Gao, Y. Li, *J. Catal.* 279 (2011) 111–122.
- [28] J.B. Laizet, A.K. Søiland, J. Leglise, J.C. Duchet, *Catal.* 10 (2000) 89–97.
- [29] L. Baraket, A. Ghorbel, P. Grange, *Appl. Catal. B* 72 (2007) 37–43.

- [30] H.Q. Guo, C.B. Chen, Y. Xiao, J.G. Wang, Z.H. Fan, D.B. Li, Y.H. Sun, *Fuel Process. Technol.* 106 (2013) 77–83.
- [31] M. Bensitel, O. Saur, J.C. Lavalley, B.A. Morrow, *Mater. Chem. Phys.* 19 (1988) 147–156.
- [32] J. Zieliński, I. Zglinicka, L. Znak, Z. Kaszukur, *Appl. Catal. A* 381 (2010) 191–196.
- [33] N. Katada, J.-i. Endo, K.-i. Notsu, N. Yasunobu, N. Naito, M. Niwa, *J. Phys. Chem. B* 104 (2000) 10321–10328.
- [34] S.S. Akarmazyan, P. Panagiotopoulou, A. Kambolis, C. Papadopoulou, D.I. Kondarides, *Appl. Catal. B* 145 (2014) 136–148.
- [35] M. Tamura, K.-i. Shimizu, A. Satsuma, *Appl. Catal. A* 433 (2012) 135–145.
- [36] M.W. Anderson, J. Klinowski, *Zeolites* 6 (1986) 455–466.
- [37] T. Yamaguchi, T. Jin, K. Tanabe, *J. Phys. Chem.* 90 (1986) 3148–3152.
- [38] J.R. Sohn, S.H. Lee, *Appl. Catal. A* 266 (2004) 89–97.
- [39] J.E. Sambeth, M.A. Centeno, A. Paúl, L.E. Briand, H.J. Thomas, J.A. Odriozola, *J. Mol. Catal. A* 161 (2000) 89–97.
- [40] C. Li, K. Domen, K.-i. Maruya, T. Onishi, *J. Catal.* 125 (1990) 445–455.
- [41] Z. Kang, H. Ma, B. Wang, *Ind. Eng. Chem. Res.* 48 (2009) 9346–9349.
- [42] I. Kim, J. Kim, D. Lee, *Appl. Catal. B* 148 (2014) 295–303.
- [43] Y.H. Lei, Q. Sun, Z.X. Chen, J.Y. Shen, *Acta Chim. Sinica* 67 (2009) 767–772.
- [44] J.-M. Tatibouët, H. Lauron-Pernot, *J. Mol. Catal. A* 171 (2001) 205–216.